bioRxiv preprint doi: https://doi.org/10.1101/2022.06.14.496195; this version posted June 17, 2022. The copyright holder for this preprint (which was not certified by peer review) is the author/funder. All rights reserved. No reuse allowed without permission.

Inhibition of Fas Receptor Endocytosis Sensitizes Cancer Cells to Fas-induced Apoptosis

Mehmet H. Kural[1,2,*], Umidahan Djakbarova[3], Bilal Cakir[4], Yoshiaki Tanaka[4,5], Yasaman Madraki[3], Hong Qian[1,2], Jinkyu Park[6], Lorenzo R. Sewanan[7], Comert Kural [3,8,*], Laura E. Niklason[1,2,*]

[1] Department of Anesthesiology, School of Medicine, Yale University, New Haven, CT, 06519, USA.

[2] Present address: Humacyte Inc., Durham, NC, 27213, USA.

[3] Department of Physics, The Ohio State University, Columbus, OH, 43210, USA.

[4] Department of Genetics, Yale Stem Cell Center, Yale School of Medicine, New Haven, CT, 06519, USA.

[5] Present address: Department of Medicine, Maisonneuve-Rosemont Hospital Research Center, University of Montreal, Montreal, QC, H1T 2M4, Canada.

[6] Yale Cardiovascular Research Center, Department of Internal Medicine, School of Medicine, Yale University, New Haven, CT, 06519, USA.

[7] Department of Internal Medicine, Columbia University, New York, NY, 10032, USA.

[8] Interdisciplinary Biophysics Graduate Program, The Ohio State University, Columbus, OH 43210, USA.

* To whom correspondence should be addressed.

bioRxiv preprint doi: https://doi.org/10.1101/2022.06.14.496195; this version posted June 17, 2022. The copyright holder for this preprint (which was not certified by peer review) is the author/funder. All rights reserved. No reuse allowed without permission.

Abstract

Fas (CD95/APO-1) is a transmembrane death receptor that transduces apoptotic signals upon binding to its ligand and assembling into a death-inducing signaling complex (DISC) (*1*, *2*). Intracellular trafficking of Fas receptors, including recycling from endosomes to the plasma membrane, plays a vital role in ligand-induced assembly of DISC (*3*, *4*). Although Fas is highly expressed in tumor cells (*5*, *6*), insufficient expression of these receptors on the cell surface makes cancer cells insensitive to the Fas-induced apoptosis (*4*, *7–9*). Here we show that inhibition of endocytosis increases the formation of Fas microaggregates on the plasma membrane and sensitizes cancer cells to Fas-induced apoptosis. We have identified a clinically used vasodilator, Fasudil, that slows down endocytosis by increasing plasma membrane tension. Fasudil enhanced apoptosis in cancerous cells when combined with exogenous soluble Fas ligand (FasL), whereas the synergistic effect was substantially weaker in nonmalignant cells. Additionally, the FasL and Fasudil combination prevented glioblastoma cell growth in embryonic stem cell-derived brain organoids and induced tumor regression in a xenograft U87 tumor model in nude mice. Our results demonstrate that FasL treatment has strong potential as an apoptosis-directed cancer therapy when the formation of Fas microaggregates is augmented by slowing down endocytosis dynamics.

bioRxiv preprint doi: https://doi.org/10.1101/2022.06.14.496195; this version posted June 17, 2022. The copyright holder for this preprint (which was not certified by peer review) is the author/funder. All rights reserved. No reuse allowed without permission.

Main

Fas (CD95/APO-1) is a tumor necrosis factor superfamily death receptor that regulates immune system homeostasis (*10*). Upon ligation at the plasma membrane, Fas receptors cluster into a death-inducing signaling complex (DISC) that activates caspase-8 to initiate a downstream signaling cascade giving rise to apoptosis (*1*). Since Fas is highly expressed in numerous cancer types, several attempts have targeted apoptotic pathways in tumor cells (*11–16*). However, the development of a systemic therapy utilizing exogenous soluble Fas ligand (FasL) has been unfeasible as tumors develop resistance to Fas-induced apoptosis (*6*, *17*, *18*). Moreover, in contrast to its canonical function, Fas signaling is associated with increased proliferation and metastasis in several cancer types (*19*).

Insufficient Fas expression on the cell surface is one of the mechanisms that make cancer cells insensitive to Fas-induced apoptosis (*4*, *7–9*). Cancer cells execute multiple strategies to reduce the surface levels of Fas receptors. Tumor cells lacking functional p53 fail to transport Fas from the Golgi complex to the plasma membrane (*20*). Fas receptors endocytosed from the cancer cell surface are predominantly delivered to lysosomes for degradation, instead of recycling back to the plasma membrane (*4*). For these reasons, we hypothesized that the susceptibility of cancer cells to Fas-induced apoptosis can be enhanced by slowing down the endocytic machinery that internalizes Fas receptors from the plasma membrane. Increased density of Fas receptors in the presence of FasL is expected to increase the likelihood of ligation and DISC formation (Fig. 1a).

Mechano-inhibition of endocytosis dynamics by Fasudil

Endocytosis of membrane receptors and their ligands from the plasma membrane has regulatory roles in a myriad of cellular processes including signal transduction and intercellular

bioRxiv preprint doi: https://doi.org/10.1101/2022.06.14.496195; this version posted June 17, 2022. The copyright holder for this preprint (which was not certified by peer review) is the author/funder. All rights reserved. No reuse allowed without permission.

communication (*21*, *22*). Cells utilize distinct endocytic machinery to produce the work necessary for transforming flat membrane patches into highly curved endocytic pockets and vesicles (*23–26*). Curvature generation on the plasma membrane is hindered by mechanical tension, which is a potent and reversible regulator of endocytosis dynamics in cells (*26–30*). Interruption of endocytosis through different means, including increased membrane tension, can alter the plasma membrane proteome significantly (*31*) and, consequently, regulate various cellular and organismal processes (*32–35*). It is shown that cancer cells alter their endocytic mechanisms to reduce the surface expression of proteins (*36–38*), including death receptors, to avoid apoptosis (*39*, *40*). Interestingly, the membrane tension of cancer cells is significantly lower than their nonmalignant counterparts (*41*, *42*). While lower membrane tension may give rise to the "dysregulated" or "derailed" endocytosis reported in cancer cells (*43*, *44*), it is expected to make cancer cells more susceptible to mechanical perturbations targeting endocytosis dynamics (*41*, *42*).

In this study, to test whether we can increase the surface expression of Fas receptors in cancer cells, we investigated strategies to impede endocytosis dynamics mechanically, i.e., by increasing plasma membrane tension (*27–30*), rather than targeting endocytic machinery directly due to the toxic side effects of chemical endocytosis inhibitors. It has been shown that reduced actomyosin contractility in cells gives rise to increased plasma membrane tension (*45*, *46*). In good agreement with these reports, we found that treating triple-negative breast cancer (SUM159) cells with Fasudil, a clinically available Rho-kinase inhibitor prescribed as a vasodilator (*47*), results in a significant increase in the membrane tether forces measured by optical tweezers (Fig. 1a, b). To assess the effects on endocytosis, we monitored the dynamics of clathrin-coated endocytic carriers using spinning-disk fluorescence microscopy (*48*, *49*). As expected, we observed that endocytic clathrin coats at the adherent surface of SUM159 cells became more static upon Fasudil treatment

bioRxiv preprint doi: https://doi.org/10.1101/2022.06.14.496195; this version posted June 17, 2022. The copyright holder for this preprint (which was not certified by peer review) is the author/funder. All rights reserved. No reuse allowed without permission.

(Fig. S1a). Using a more quantitative assessment, we found that the standard deviation (SD) of clathrin coat growth rates reduced significantly, a robust indicator of slower endocytosis dynamics (*50*) (Fig. 1c). Overall, our results demonstrate that endocytosis dynamics can be slowed down mechanically in cells using Fasudil, a clinically used rho-kinase inhibitor.

Inhibition of endocytosis increases formation of Fas microaggregates on the cell surface

It has been shown that aggregation of Fas receptors in plasma membrane microdomains before ligation increases the efficiency of DISC formation upon FasL stimulation (*51*, *52*). We investigated the effects of endocytosis inhibition on the density and distribution of Fas receptors in glioblastoma (U87), small lung carcinoma (A549), liver carcinoma (HepG2), prostate cancer (PC3), and triple-negative breast cancer (SUM159) cells along with non-cancerous human umbilical vein endothelial (HUVEC) cells using immunofluorescence imaging. We found that the immunofluorescence signal of Fas was significantly higher in cancer cells compared to HUVECs. Fas receptors were observed as bright punctae on the surface of the cancer cells, indicating the formation of microaggregates (Fig. 1d; Supplementary Video 1). Furthermore, when endocytosis dynamics were hampered for two hours by 40 μM Fasudil treatment, the Fas signal density has increased by ~2-fold on the surface of the cancer cell lines, whereas no effect was observed in HUVECs (Fig. 1d-f).

To corroborate our findings, we also tested the formation of Fas microaggregates in cells treated with blebbistatin or dyngo-4a that are expected impede endocytosis dynamics mechanically and chemically, respectively. Blebbistatin is a myosin-II inhibitor that is used for reducing actomyosin contractility in cells (*53*). Similar to Fasudil treatment, reduced contractility by blebbistatin also gives rise to increased plasma membrane tension (*45*, *46*). On the other hand,

bioRxiv preprint doi: https://doi.org/10.1101/2022.06.14.496195; this version posted June 17, 2022. The copyright holder for this preprint (which was not certified by peer review) is the author/funder. All rights reserved. No reuse allowed without permission.

dyngo-4a inhibits receptor endocytosis directly by targeting the dynamin GTPase that is required for the scission of endocytic vesicles (*54*). We aimed to minimize the concentration of dyngo-4a to limit its off-target effects and found that clathrin-mediated endocytosis dynamics slow down significantly upon 5 μM dyngo-4a treatment (Fig. S1b). In good agreement with the Fasudil assays, 2-hours incubation of cancer cells with 10 μM blebbistatin or 5 μM dyngo-4a resulted in a significant increase in the Fas signal density within the cancer cell lines, whereas no increase was observed in HUVECs (Fig. 1g, h).

We found that Fasudil or dyngo-4a treatments have no effect on the total Fas protein expression levels (Fig. S2a). To test whether the increase in the density of Fas signal takes place exclusively on the cell surface, we used spinning disk confocal imaging to restrict our analyses to the ventral/adherent surface of the plasma membrane. We used adaptor protein 2 (AP2, a clathrin adaptor localizing to the plasma membrane exclusively) signal to confirm that the imaging plane coincides with the plasma membrane (Fig. S2b). We found that inhibition of endocytosis through Fasudil or dyngo-4a treatment has no major effect on the density of the microaggregates (Fig. S2c). However, the immunofluorescence intensity of the microaggregates increased up to an order of magnitude on the surface of the cancer cells. Whereas no increase was observed in HUVECs and HBE cells (Fig. S2d). Overall, our analyses show that, in good agreement with our hypothesis, inhibition of endocytosis increases the surface availability of Fas receptors, which form microaggregates on the surface of cancer cells.

Inhibition of endocytosis sensitize cancer cells to soluble Fas ligand

After confirming that inhibition of endocytosis increases the growth of Fas microaggregates, we tested whether this strategy sensitizes cancer cells to exogenous FasL. To this

bioRxiv preprint doi: https://doi.org/10.1101/2022.06.14.496195; this version posted June 17, 2022. The copyright holder for this preprint (which was not certified by peer review) is the author/funder. All rights reserved. No reuse allowed without permission.

end, we assessed the viability of cells under distinct conditions by quantifying the ATP level present in the cell culture medium at the 48th hour of the treatment. When human recombinant FasL (400 ng/mL) was added to the culture medium alone, it had a mild to moderate effect on cancer cell viability (55.6%, %80.2, 58.0%, 67.8%, 44.6%, and 59.9% of the control in U87, PC3, BT549, A549, HepG2, and SUM159 cells, respectively). However, inhibition of endocytosis and raising the surface density of Fas microaggregates via 40 μM Fasudil treatment increased the effect of FasL and decreased the cell viability substantially for each cell type (3.6-24.2%) (Fig. 2a-c; Fig. S3a). We observed that 10 μM blebbistatin treatment, instead of Fasudil, also resulted in the same synergistic effect in U87 cells (Fig. 2c). We have also used alternative, chemical and mechanical, approaches to slow down endocytosis temporarily and monitored the effects on the sensitivity of U87 cells to FasL. First, we treated the cells with 5 μM dyngo-4a and 400 ng/mL FasL combination for only 30 minutes and, subsequently, incubated cells in culture medium containing 400 ng/mL FasL only until quantifying the viability at the 48th hour. We found that even a transient inhibition in endocytosis dynamics reduced cell viability radically in the presence of FasL (Fig. 2c). We observed the same outcome using 2 μM pitstop-2, a potent inhibitor of clathrin-dependent and independent endocytic pathways (Fig. S1b, c), instead of dyngo-4a to hinder endocytosis dynamics in cancer cells temporarily (Fig. S4a). Whereas HUVECs were affected minimally by both treatments (Fig. S4b). The second approach relied on a purely mechanical interference with endocytosis dynamics: to increase membrane tension temporarily, we incubated cells with 400 ng/mL FasL in 80% hypotonic culture medium for 30 minutes. Hypo-osmotic swelling during this period results in increased cell membrane tension and, therefore, slower endocytosis dynamics (*28*, *30*, *55*). We have then reverted the culturing conditions to isotonic medium (100% culture medium) containing 400 ng/mL FasL to cease mechano-inhibition of endocytosis during the rest of the experiment. Quantification of the cell viability at the 48th hour revealed that even a

bioRxiv preprint doi: https://doi.org/10.1101/2022.06.14.496195; this version posted June 17, 2022. The copyright holder for this preprint (which was not certified by peer review) is the author/funder. All rights reserved. No reuse allowed without permission.

temporary interference with the endocytosis of Fas receptors significantly increased sensitivity of cancer cells to exogenous FasL (Fig. 2c).

Remarkably, viability of HUVECs, HBE cells, and induced pluripotent stem cell (iPS)-derived cardiomyocytes were affected by Fasudil and FasL combination relatively minimally compared to cancer cells (93.1%, 73.1%, and 83.2% of the control, in HUVECs, HBE cells, and iPS-derived cardiomyocytes, respectively) (Fig. 2d; Fig. S3b; Supplementary Video 2 and 3). These results demonstrate that targeting endocytosis increases the sensitivity of cancer cells to FasL while sparing endothelial cells, bronchial epithelial cells, or cardiomyocytes. As the next step, we wanted to assess whether this approach can be transformed into a targeted cancer therapy by testing it on physiologically relevant contexts, i.e., cortical brain organoids and xenograft tumors.

Application of Fasudil - FasL combination on cortical brain organoids with U87 glioblastoma

We generated an *in vitro* glioblastoma model based on embryonic stem cell-derived cortical brain organoids including U87 glioblastoma cells labeled with red fluorescent protein (RFP), which allowed us to visualize and quantitatively assess the changes in the glioblastoma mass within the organoids (*56*) (Fig. 3a). Treatment with Fasudil - FasL combination did not increase the percentage of apoptotic cells in 78-day-old brain organoids that do not contain U87 cells (Fig. S5). When we treated U87 cell-containing brain organoids with Fasudil - FasL combination for three days, the volume occupied by RFP-labeled U87 cells decreased dramatically, leaving behind an acellular space (Fig 3b, c). We also found that both untreated and drug-treated organoids express neuron progenitor marker SOX2 and differentiated neural marker TUJ1 (anti-β-Tubulin III) staining. These results demonstrate that the Fasudil - FasL combination

bioRxiv preprint doi: https://doi.org/10.1101/2022.06.14.496195; this version posted June 17, 2022. The copyright holder for this preprint (which was not certified by peer review) is the author/funder. All rights reserved. No reuse allowed without permission.

can kill glioblastoma cells in brain organoids selectively with minimal effect on the viability of neuron progenitor cells.

To assess the effect of Fasudil – FasL combination on U87 glioblastoma cells in brain organoids with single-cell resolution, we used single-cell transcriptome analysis of a total of 1391, 1097, and 2149 cells derived from organoids that are untreated, treated for 24 hours, and 72 hours, respectively. We identified 21 clusters that were systematically assigned to 13 cell types, including neurons, astrocytes, neural progenitor cells, and glioblastoma cells (Fig. 3d-e). UMAP plots show that the number of glioblastoma cells decreased dramatically after 24 hours of treatment and became negligible at 72 hours (Fig. 3f-g). Global comparison of the transcriptome between FasL and Fasudil combination- and non-treated organoids identified that 611 and 252 genes are significantly up- and down-regulated by the treatment, respectively. Gene ontology analysis identified that the up-regulated genes are involved in oxidative stress response (e.g., *GCLM*, *HSF1*, and *OGG1*) and apoptosis (e.g., *MSH6*, *DNAJA1*, and *TRAP1*) and DNA repair (e.g., *FOXO4*, *MDM4*, and *CUL4A*) (FDR < 0.05 by hypergeometric test). In contrast, metabolic genes for glycoprotein (e.g., *MVD*, *OST4*), ATP (e.g., *COX5B*, *COX6C*), sterol (e.g., *NPC1*, *NPC2*) and collagen (e.g., *MMP2*, *VIM*) are significantly downregulated (FDR < 0.05) (Fig. 3h). However, with treatment, the upregulation of cell death-related genes and down regulation of metabolic genes were much stronger in glioblastoma cells than those in non-cancer cells as a whole, neuron, and neuron progenitor cells. Interestingly, both apoptotic and metabolic genes were upregulated in astrocytes upon the treatment (Fig. 3h).

bioRxiv preprint doi: https://doi.org/10.1101/2022.06.14.496195; this version posted June 17, 2022. The copyright holder for this preprint (which was not certified by peer review) is the author/funder. All rights reserved. No reuse allowed without permission.

Combination therapy of U-87 glioblastoma *in vivo* xenografted tumors with Fasudil and FasL

We further evaluated the anti-tumor efficacies of Fasudil and FasL as monotherapies or in combination *in vivo* using a U87 xenograft tumor model in athymic nude mice. In our first study, when the drugs were administered intraperitoneally, no significant differences in tumor growth were observed in the treatment arms compared to the vehicle arm (Fig. S6). In the next trial, the drugs were administered via an intratumoral route in an attempt to increase local concentrations of the drugs. After two weeks of intratumoral administration, the route was switched to intraperitoneal due to observation of trauma and tissue dehiscence the injection sites. One month after the tumor initiation and completion of seven therapy cycles, the combination treatment arm showed significant tumor inhibition compared to the vehicle as well as the monotherapy arms (Fig. 4a, b). The median survival ranged from to 27-28 days in the vehicle and the monotherapy arms with less than 40% of the animals surviving one month after implantation. One month post implantation, none of the mice in the combination treatment arm reached endpoint and tumor growth was observed in only one mouse. Fifty-percent (4/8) of the treated mice showed tumor volume regression and notably, one of the mice was cured (complete tumor regression) after the fifth injection of the Fasudil - FasL combination (Fig. 4d). The less than 100% survival in the Kaplan Meier plot is due to non-tumor size related, inexplicable death of one mouse in this group in the middle of the study (Fig. 4c). These results demonstrate that local administration of Fasudil - FasL combination, but not Fasudil or FasL alone, has a significant tumor suppressing effect and possibly curative *in vivo*.

bioRxiv preprint doi: https://doi.org/10.1101/2022.06.14.496195; this version posted June 17, 2022. The copyright holder for this preprint (which was not certified by peer review) is the author/funder. All rights reserved. No reuse allowed without permission.

Conclusion

Cancer cells develop mechanisms to exploit Fas expression as a survival factor while circumventing Fas-induced apoptosis (*19*). Our study aimed towards sensitization of cancer cells to Fas-induced apoptosis to transform their survival strategy into a targeted cancer therapy. We show that inhibition of endocytosis, either chemically through the application of small molecule inhibitors or mechanically by increasing plasma membrane tension, promotes the growth of Fas microaggregates on the cell surface and diminishes cancer cells' resistance to FasL. In physiological contexts, this mechanism can be activated by Fasudil, a clinically used Rho-kinase inhibitor that slows down endocytosis in cancer cells. Overall, our results in cortical organoids and mouse xenograft tumor models demonstrate that FasL can be utilized as a potent and selective anticancer drug when combined with Fasudil.

Methods:

hESCs culture

BC4 hESCs (*56*) were cultured on Matrigel (BD Biosciences) coated dishes with mTeSR1 media (Stem Cell Technologies) and passaged every week by disassociating with 0.83 U/mL Dispase (Stem Cell Technologies). All experiments including hESCs were approved by Yale Embryonic Stem Cell Research Oversight (ESCRO).

Cancer cell culture

U87, A549, and HepG2 cell lines were purchased from ATCC and were cultured in DMEM supplemented with 10% FBS and 1% pen/strep (Thermo Fischer). PC3 and BT549 cells were donated by Yale Center for Precision Cancer Modeling (YCPCM) and cultured in F-12 (Thermo

bioRxiv preprint doi: https://doi.org/10.1101/2022.06.14.496195; this version posted June 17, 2022. The copyright holder for this preprint (which was not certified by peer review) is the author/funder. All rights reserved. No reuse allowed without permission.

Fischer) or RPMI (Thermo Fischer) media supplemented with 10% FBS and 1% pen/strep, respectively. SUM159 cells genome edited to express AP2-EGFP were donated by Tomas Kirchhausen's group at Harvard Medical School (*49*). SUM159 cells were cultured in F-12 media supplemented with 5% FBS, 1% pen/strep, 1mg/ml hydrocortisone (Sigma Aldrich) and 10mg/ml insulin (Sigma Aldrich). Cells were passaged every two days with trypsin treatment. In viability experiments, cells were treated with different combinations of 400 ng/mL human recombinant Fas ligand (Biolegend), 40 μM Fasudil HCl (SellekChem), 10 μM Blebbistatin (Sigma), 5 μM Dyngo-4a (Cayman Chemical), or 2 μM Pitstop-2 (Abcam) in 96-well plates for 48 hours. Cell viability was quantified by detection of ATP content in the culture medium with CellTiter-Glo® Luminescent Cell Viability Assay (Promega) by following the manufacturer's instructions.

Immunofluorescence microscopy and image analysis

Cells were fixed with 3.7% paraformaldehyde (Sigma-Aldrich), permeabilized with 0.1% Triton X-100 (Fisher Biotech, Hampton, NH, USA), and then blocked with PBS supplemented with goat serum (2%, v/v) (Southern biotech) and 0.1% Tween-20 (Thermo Fischer). Cells were then incubated with FAS Mouse anti-Human (Clone: 4F8H6, Invitrogen) at 1:500 dilution and appropriate fluorochrome-conjugated secondary antibody (Alexa Fluor 647 anti-mouse IgG1, Fischer Scientific) for CD-95 immunostaining.

For quantitative analysis of cell surface-associated CD95 expression, fluorescent images of the immunostained cells were collected using Nikon TIE fluorescence microscope equipped with a CSU-W1 spinning disk unit (Yokogawa Electric Corporation), a 100× objective lens (Nikon CFI Plan-Apochromat Lambda, NA 1.45), a sCMOS camera (Prime 95B; Teledyne Photometrics), and 488- and 640-nm excitation lasers with 100 mW of nominal power. Images were acquired at a rate

bioRxiv preprint doi: https://doi.org/10.1101/2022.06.14.496195; this version posted June 17, 2022. The copyright holder for this preprint (which was not certified by peer review) is the author/funder. All rights reserved. No reuse allowed without permission.

of 0.25–0.5 Hz with a laser exposure of 100 ms per frame. Image acquisition was performed using NIS Elements software.

A comparative analysis of CD95 expression was conducted using Fiji software (https://imagej.net/Fiji/Downloads) by quantifying signal intensities obtained from confocal sections. To quantify the number, size, and area fraction of CD95 puncta, the surface area of each cell was demarcated and subsequently masked to create binary images by using the 'analyze particles' function of the same software (*57*). After background subtraction, original image sections were multiplied by the mask obtained from the same field of view. For each cell, the mean intensity of spots was calculated by dividing the integrated intensity of the selected area by the number of detected spots.

Membrane tether force measurements

Membrane tether force measurements were conducted at 37° C using C-Trap optical tweezers system (LUMICKS, Amsterdam, The Netherlands). SUM159 cells gene-edited to express AP2–eGFP (*49*) were plated in a custom-designed flow chamber 15-24 hours prior to the experiments and incubated them at 37°C and 5% CO_2. The flow chamber was composed of a microscope cover glass (No 1.5, Fisher Scientific), a layer of parafilm tape as a separator, and a 1.0 mm thick microscope slide (Fisher Scientific). This selection of thickness for cover glass, parafilm, and the glass slide is designed for the flow channel to be compatible with the working distance of our C-Trap objective and condenser.

Tethers were pulled from the plasma membrane after creating contact with streptavidin-coated polystyrene beads with a mean diameter of 1.87 µm (SVP-15, Spherotech). Right before the experiments, the growth medium was replaced with the imaging medium (containing the beads)

bioRxiv preprint doi: https://doi.org/10.1101/2022.06.14.496195; this version posted June 17, 2022. The copyright holder for this preprint (which was not certified by peer review) is the author/funder. All rights reserved. No reuse allowed without permission.

and, subsequently, flow channel inlet and outlet were sealed. The imaging medium was prepared by diluting the bead suspension down to 0.01% w/v, spinning and resuspending them once in PBS and then in phenol red-free L15 medium (Thermo Fisher Scientific) supplemented with 10% FBS.

The trap stiffness was calibrated using the thermal noise spectrum. After calibration, the stage is moved at 1μm/s speed until the bead is in contact with the cell. After 4-10 seconds, the stage is moved in the opposite direction at 5μm/s speed to attain a tether length of 10μm. The tether is then held stationary for ~20 seconds to measure the static tether force as described previously (*58*).

Imaging clathrin-mediated endocytosis dynamics in live cells

Fluorescence imaging was performed using Nikon TIE fluorescence microscope equipped with a CSU-W1 spinning disk unit (Yokogawa Electric Corporation), a 100× objective lens (Nikon CFI Plan-Apochromat Lambda, NA 1.45), a sCMOS camera (Prime 95B; Teledyne Photometrics), and 488 nm excitation lasers with 100 mW of nominal power and temperature controlled chamber. NIS Elements image acquisition software was used for acquisition of 2D time-lapse movies.

Endocytic clathrin dynamics was captured in SUM159 cells genome edited to express AP2-EGFP (*49*). 15-24 hours prior to imaging, cells were plated on a glass bottom dish (MatTek Life Sciences) and incubated at 37ºC with 5% CO_2. Cells were imaged in phenol red-free L15 medium (Thermo Fisher Scientific) supplemented with 10% FBS at a rate of 0.25 Hz with laser exposure of 100 ms per frame. Two-dimensional time-lapse movies were acquired using NIS Elements software.

Individual clathrin-coated structures were captured and endocytic events were detected using the TraCKer software (*50*, *59*). Clathrin coat growth rate analysis was conducted was previously described (*50*) to assess the changes in clathrin-mediated endocytosis dynamics.

bioRxiv preprint doi: https://doi.org/10.1101/2022.06.14.496195; this version posted June 17, 2022. The copyright holder for this preprint (which was not certified by peer review) is the author/funder. All rights reserved. No reuse allowed without permission.

Western Blot

U87 cells, cultured on tissue culture plates in standard culture medium with or without 40 μM Fasudil, were lysed in cold RIPA buffer (50 mM Tris-HCl, pH 7.4, 150 mM NaCl, 1% [v/v] Triton X-100, 0.5% [w/v] SDC, and 0.1% [w/v] sodium dodecyl sulphate (SDS)) containing 1% protease inhibitor (Sigma Aldrich, St. Louis, MO). Protein lysate was mixed with Laemmli sample buffer, reduced (DTT at 95 °C 5 min), and loaded on 4–20% gradient polyacrylamide gels (Bio-Rad, Hercules, CA). Blots were run for 60 min at 120 V and the protein was transferred to PVDF membrane and blocked for 20 minutes at room temperature in 3% nonfat dry milk. Anti-FAS primary antibody (Proteintech, Rosemont, IL, USA) with 0.2 μg/mL concentration was applied overnight at 4 °C in 1% nonfat dry milk in TBST buffer (0.1% Tween-20 in Tris-buffered saline). After being rinsed with TBST, goat anti rabbit secondary antibody (Novus Biologicals, Centennial, CO, USA) were applied at a dilution of 1:10,000 for 1 hour at RT. Protein was detected using enhanced chemiluminescence (Thermo Scientific, Waltham, MA, USA).

Glioblastoma model in cortical brain organoids

As described previously (*56*), hESCs were dissociated into single cells via Accutase and 9,000 cells, containing 0.5% RFP-infected U87 cells were plated into a well of U-bottom ultra-low-attachment 96-well plates. Neural induction medium (DMEM-F12, 15% (v/v) KSR, 5% (v/v) heat-inactivated FBS (Life Technologies), 1% (v/v) Glutamax, 1% (v/v) MEM-NEAA, 100 μM β-mercaptoethanol, 10 μM SB-431542, 100 nM LDN-193189, 2 μM XAV-939 and 50 μM Y27632) was used as culture media for ten days. Organoids were transferred to organoids were transferred to ultra-low-attachment six-well plate in hCO media without vitamin A (1:1 mixture of DMEM-F12 and Neurobasal media, 0.5% (v/v) N2 supplement, 1% (v/v) B27 supplement without vitamin

bioRxiv preprint doi: https://doi.org/10.1101/2022.06.14.496195; this version posted June 17, 2022. The copyright holder for this preprint (which was not certified by peer review) is the author/funder. All rights reserved. No reuse allowed without permission.

A, 0.5% (v/v) MEM-NEAA, 1% (v/v) Glutamax, 50 μM β-mercaptoethanol, 1% (v/v) penicillin/streptomycin and 0.025% insulin) at day ten and the media was changed every other day. At day 18, Vitamin A, brain-derived neurotrophic factor, and ascorbic acid were added to the culture medium. Organoids with or without glioblastoma were treated with Fas ligand-Fasudil combination after Day 75 for 72 hours for viability studies.

Immunofluorescence microscopy and image analysis for organoids

Organoids were fixed in 3.7% paraformaldehyde at 4 °C overnight followed by three washes with PBS at room temperature. Then, organoids were incubated in a 30% sucrose solution for 2 days at 4 °C. Organoids were equilibrated with optical cutting temperature compound at RT for 15 minutes, transferred to base molds, and embedded in optical cutting temperature compound on dry ice. Then, 40-μm cryosections were generated, and organoid blocks were stored at −80 °C. Slides were dried for 2 hours at RT and incubated with 0.1% Triton-100 for 15 minutes at RT in a humidified chamber. Organoids were blocked with 3% BSA at room temperature for 2 hours, and then were incubated with the primary antibodies (mouse anti-Sox-2 and rabbit anti-TUJ-1) diluted 1:100 in 3% BSA overnight at 4 °C. After two washing steps, organoids were incubated with Alexa Fluor Dyes (1:500) for 1 hour following nuclei staining with DAPI (1:1,000). Finally, slides were mounted with ProLong Gold Antifade Reagent and images were taken with another CSU-W1 spinning disk unit (Yokogawa Electric Corporation), a 20× objective lens (CFI Plan Apochromat Lambda 20x/0.75, WD 1 mm, No: MRD00205), an Andor iXon camera (Ultra888 EMCCD, 1024x1024 (pix), 13 um pixel), and 488-, 550-, and 640-nm excitation lasers with 100 mW of nominal power. The DNA strand breaks were detected with TUNEL stain (11684795910, Sigma) was performed to detect apoptotic or dead cells following the manufacturer's protocol. The ratio of the mean signal intensity for TUNEL stain to DAPI was calculated for each image.

bioRxiv preprint doi: https://doi.org/10.1101/2022.06.14.496195; this version posted June 17, 2022. The copyright holder for this preprint (which was not certified by peer review) is the author/funder. All rights reserved. No reuse allowed without permission.

Data processing of single-cell RNA-seq

Single-cell RNA-seq reads were mapped to GRCh38 human genome (GRCh38-2020-A) and counted with Ensembl genes by count function of CellRanger software (v3.0.2) with default parameters. Batch effect and intrinsic technical effects were normalized by Seurat (v3.0.2) (*60*). Briefly, we filtered out cells with less than 50 detected genes and more than 15% of mitochondria-derived reads as low-quality samples. Raw UMI count was normalized to total UMI count in each library. Top 2,000 highly variable genes were used to identify cell pairs anchoring different scRNA-seq libraries using 20 dimensions of canonical correlation analysis. All scRNA-seq libraires used in this study were integrated into a shared space using the anchor cells. After scaling gene expression values across all integrated cells, we performed dimensional reduction using principal component analysis (PCA). For the visualization, we further projected single cells into two-dimensional UMAP space from 1st and 20th PCs. Graph-based clustering was then implemented with shared nearest neighbor method from 1st and 20th PCs and 0.8 resolution value. Differentially-expressed genes (DEGs) in each cluster was identified with more than 1.25-fold change and $p<0.05$ by two-sided unpaired T test. Gene Ontology analysis was performed to the DEGs by GOstats Bioconductor package (v2.46.0) (*61*). False discovery rate was adjusted by p.adjust function in R with “method=”BH”” parameter.

Cluster labeling was performed by unique markers, Gene Ontology, and enrichment of gene signatures as described previously (*56*, *62*). Briefly, neuronal and non-neuronal clusters were separated by neuronal growth cone (*STMN2*, *GAP43*, and *DCX*) and early neurogenesis markers (*VIM*, *SOX2* and *HES1*). Neuronal clusters are further classified into excitatory and inhibitory neurons by expression of glutamate (*vGLUT1/2*) and GABA transporters (*vGAT*), respectively. In addition, neurons expressing neuroblast markers (*NEUROD1/6*) were labeled as intermediate

bioRxiv preprint doi: https://doi.org/10.1101/2022.06.14.496195; this version posted June 17, 2022. The copyright holder for this preprint (which was not certified by peer review) is the author/funder. All rights reserved. No reuse allowed without permission.

progenitor cells (IPCs), which are transitioning to newborn neurons (*63*). Non-neuronal clusters are classified into mitotic and non-mitotic cells with presence and absence of cell cycle-related gene expression, respectively. The mitotic clusters were labeled as NPC S, NPC S/G1, or NPC G1 by S (*PCNA*, *MCM2*) and G1 phase markers (*TOP2A*, and *MKI67*). The non-mitotic clusters with significant overrepresentation of a GO term "Astrocyte differentiation (GO:0048708)" were assigned to astrocytes. Astrocyte clusters with high expression of *GFAP* and *S100B* were further labeled as mature astrocytes. *HOPX*-expressing non-mitotic clusters were assigned to radial glia cells. A non-mitotic cluster without astrocyte marker expression, but with significant overrepresentation of "glial cell development (GO:0021782)" was labeled as glial progenitor cell. Neuroepithelial cells were assigned by expression of its markers (*PLP1* and *SOX3*). Glioblastoma cluster was assigned by unique expression of GBM biomarkers (*CD44*, *ALDH1A3*, *CAVIN1*, and *MT1E*). Global comparison of transcriptome profiles was performed by 1.25-fold average expression difference and $p<0.05$ of two-sided unpaired T test between 72h-treated and non-treated organoids.

Fasudil and FasL combination therapy in U87 glioblastoma xenograft tumors

Ten million U-87 glioblastoma cells (ATCC) were implanted subcutaneously into the right flank of immune deficient athymic nude mice (Jackson Labs) in 1:1 mix of plain growth media and Matrigel (Corning). After approximately one week post transplantation when the tumors were palpable, with tumor volumes ranging from 50-200 mm^3 7-8 tumor bearing mice were randomly assigned to the following four treatment arms: Vehicle (PBS), FasL monotherapy, Fasudil monotherapy and Fasudil-FasL combination. On Mondays and Thursdays, the Fasudil monotherapy and the Fasudil-FasL combination arms received a priming dose of 50 mg/kg Fasudil, while FasL only and PBS group received an equivalent volume of PBS injection. Twenty-

bioRxiv preprint doi: https://doi.org/10.1101/2022.06.14.496195; this version posted June 17, 2022. The copyright holder for this preprint (which was not certified by peer review) is the author/funder. All rights reserved. No reuse allowed without permission.

four hours after the priming injections, PBS, FasL (180 μg/kg), Fasudil (50 mg/kg) or Fasudil (50 mg/kg) and Fas-L (180 μg/kg) in combination, was administered to the relevant arms. In the first study, the route of administration was intra-peritoneal for the entire study. In the second study, the route of drug administration was intra-tumoral to the central tumor mass for two weeks but switched to intra-peritoneal due to observation of trauma and tissue dehiscence at the injection sites. Tumor dimensions were recorded by caliper measurements at three-day intervals and volumes calculated using the formula: length x width^2/2. Treatment was ceased and the mice were euthanized after endpoint volume of 1000 mm^3 was reached in the vehicle arm. Tumors were excised from mice from all arms and images taken at the end of the study.

References:

1. F. C. Kischkel *et al.*, *EMBO J.* **14**, 5579–5588 (1995).
2. S. Nagata, *Cell*. **88**, 355–365 (1997).
3. S. Schütze, V. Tchikov, W. Schneider-Brachert, *Nat. Rev. Mol. Cell Biol.* **9**, 655–662 (2008).
4. S. Sharma *et al.*, *Nat. Commun.* **10** (2019), doi:10.1038/s41467-019-11025-y.
5. A. Algeciras-Schimnich *et al.*, *Proc. Natl. Acad. Sci. U. S. A.* **100**, 11445–11450 (2003).
6. M. E. Peter, P. Legembre, B. C. Barnhart, *Biochim. Biophys. Acta - Rev. Cancer*. **1755**, 25–36 (2005).
7. V. N. Ivanov *et al.*, *Mol. Cell. Biol.* **23**, 3623–3635 (2003).
8. V. N. Ivanov, Z. Ronai, T. K. Hei, *J. Biol. Chem.* **281**, 1840–1852 (2006).
9. B. J. N. Winterhoff *et al.*, *Differentiation*. **83**, 148–157 (2012).
10. S. Nagata, *Annu. Rev. Genet.* **33**, 29–55 (1999).
11. B. C. Trauth *et al.*, *Science (80-.).* **245**, 301–305 (1989).
12. P. Schneider *et al.*, *J. Exp. Med.* **187**, 1205–1213 (1998).
13. A. Rensing-Ehl *et al.*, *Eur. J. Immunol.* **25**, 2253–2258 (1995).
14. D. I. O'Brien *et al.*, *Expert Opin. Ther. Targets*. **9**, 1031–1044 (2005).

bioRxiv preprint doi: https://doi.org/10.1101/2022.06.14.496195; this version posted June 17, 2022. The copyright holder for this preprint (which was not certified by peer review) is the author/funder. All rights reserved. No reuse allowed without permission.

15. B. A. Carneiro, W. S. El-Deiry, *Nat. Rev. Clin. Oncol.* **17**, 395–417 (2020).

16. J. Ogasawara *et al.*, *Nature*. **364**, 806–809 (1993).

17. M. Irmler *et al.*, *Nat. 1997 3886638*. **388**, 190–195 (1997).

18. N. Bidère, H. C. Su, M. J. Lenardo, Genetic disorders of programmed cell death in the immune system. *Annu. Rev. Immunol.* **24** (2006), pp. 321–352.

19. M. E. Peter *et al.*, *Cell Death Differ.* **22**, 549–559 (2015).

20. M. Bennett *et al.*, *Science (80-.).* **282**, 290–293 (1998).

21. S. D. Conner, S. L. Schmid, *Nature*. **422**, 37–44 (2003).

22. S. Polo, P. P. Di Fiore, *Cell*. **124**, 897–900 (2006).

23. M. P. Sheetz, *Nat. Rev. Mol. Cell Biol.* **2**, 392–6 (2001).

24. N. C. Gauthier, T. A. Masters, M. P. Sheetz, *Trends Cell Biol.* **22**, 527–35 (2012).

25. T. A. Masters, B. Pontes, V. Viasnoff, Y. Li, N. C. Gauthier, *Proc. Natl. Acad. Sci. U. S. A.* **110**, 11875–80 (2013).

26. U. Djakbarova, Y. Madraki, E. T. Chan, C. Kural, *Biol. Cell*. **0**, 1–30 (2021).

27. S. Boulant, C. Kural, J.-C. Zeeh, F. Ubelmann, T. Kirchhausen, *Nat. Cell Biol.* **13**, 1124–1131 (2011).

28. J. P. Ferguson *et al.*, *J. Cell Sci.* **130**, 3631–3636 (2017).

29. N. M. Willy *et al.*, *Mol. Biol. Cell*. **28**, 3480–3488 (2017).

30. N. M. Willy *et al.*, *Proc. Natl. Acad. Sci.* **118**, e2010438118 (2021).

31. D. Tobys *et al.*, *Traffic*. **22**, 6–22 (2021).

32. M. Bergert *et al.*, *Cell Stem Cell*. **28**, 209-216.e4 (2021).

33. H. De Belly *et al.*, *Cell Stem Cell*. **28**, 273-284.e6 (2021).

34. P.-A. Pouille, P. Ahmadi, A.-C. Brunet, E. Farge, *Sci. Signal.* **2**, ra16 (2009).

35. S. Sigismund *et al.*, *Physiol. Rev.* **92**, 273–366 (2012).

36. S. R. Elkin *et al.*, *Cancer Res.* **75**, 4640–4650 (2015).

37. S. Polo, S. Pece, P. P. Di Fiore, *Curr. Opin. Cell Biol.* **16**, 156–161 (2004).

38. P. P. Di Fiore, *Mol. Oncol.* **3**, 273–279 (2009).

39. C. R. Reis, P. H. Chen, N. Bendris, S. L. Schmid, *Proc. Natl. Acad. Sci. U. S. A.* **114**, 504–509 (2017).

40. S. L. Schmid, *J. Cell Biol.* **216**, 2623–2632 (2017).

41. K. Ren, J. Gao, D. Han, *Front. Cell Dev. Biol.* **9**, 1–13 (2021).

bioRxiv preprint doi: https://doi.org/10.1101/2022.06.14.496195; this version posted June 17, 2022. The copyright holder for this preprint (which was not certified by peer review) is the author/funder. All rights reserved. No reuse allowed without permission.

42. K. Tsujita *et al.*, *Nat. Commun.* **12** (2021), doi:10.1038/s41467-021-26156-4.

43. Y. Mosesson, G. B. Mills, Y. Yarden, *Nat. Rev. Cancer*. **8**, 835–850 (2008).

44. I. Mellman, Y. Yarden, *Cold Spring Harb. Perspect. Biol.* **5** (2013), doi:10.1101/cshperspect.a016949.

45. N. C. Gauthier, M. A. Fardin, P. Roca-Cusachs, M. P. Sheetz, *Proc. Natl. Acad. Sci. U. S. A.* **108**, 14467–72 (2011).

46. A. R. Houk *et al.*, *Cell*. **148**, 175–188 (2012).

47. Y. Feng, P. V. Lograsso, O. Defert, R. Li, *J. Med. Chem.* **59**, 2269–2300 (2016).

48. C. Kural, T. Kirchhausen, *Methods Enzymol.* **505**, 59–80 (2012).

49. F. Aguet *et al.*, *Mol. Biol. Cell*. **27**, 3418–3435 (2016).

50. J. P. Ferguson *et al.*, *J. Cell Biol.* **214**, 347–358 (2016).

51. D. Delmas *et al.*, *Oncogene*. **23**, 8979–8986 (2004).

52. J. R. Muppidi, R. M. Siegel, *Nat. Immunol.* **5**, 182–189 (2004).

53. L. Figard, A. M. Sokac, *J. Vis. Exp.* (2011), doi:10.3791/2503.

54. A. Mccluskey *et al.*, *Traffic*. **14**, 1272–1289 (2013).

55. N. M. Willy *et al.*, *Dev. Cell*. **56**, 3146-3159.e5 (2021).

56. B. Cakir *et al.*, *Nat. Methods*. **16**, 1169–1175 (2019).

57. J. Schindelin *et al.*, *Nat. Methods 2012 97*. **9**, 676–682 (2012).

58. A. Diz-Muñoz *et al.*, *PLoS Biol.* **8**, e1000544 (2010).

59. C. Kural *et al.*, *CellReports*. **2**, 1111–1119 (2012).

60. T. Stuart *et al.*, *Cell*. **177**, 1888-1902.e21 (2019).

61. S. Falcon, R. Gentleman, *Bioinformatics*. **23**, 257–258 (2007).

62. Y. Tanaka, B. Cakir, Y. Xiang, G. J. Sullivan, I. H. Park, *Cell Rep.* **30**, 1682-1689.e3 (2020).

63. S. Tutukova, V. Tarabykin, L. R. Hernandez-Miranda, *Front. Mol. Neurosci.* **0**, 109 (2021).

bioRxiv preprint doi: https://doi.org/10.1101/2022.06.14.496195; this version posted June 17, 2022. The copyright holder for this preprint (which was not certified by peer review) is the author/funder. All rights reserved. No reuse allowed without permission.

Acknowledgements:

This work was funded by AHA Postdoctoral Fellowship (17POST33661238) awarded to M.H.K., NSF Faculty Early Career Development Program (award number: 1751113) and NIH R01GM127526 to C.K., and NIH R01HL148819 to L.E.N. U.D. is supported by the Pelotonia Fellowship Program. Any opinions, findings, and conclusions expressed in this material are those of the authors and do not necessarily reflect those of the Pelotonia Fellowship Program or the Ohio State University. Authors thank Yale Center for Precision Cancer Modeling, for their help with the animal studies, and Yale West Campus Imaging Core.

Contributions:

M.H.K. oversaw the project, designed, and optimized the experiments and analyzed the data. C.K and M.H.K. prepared the manuscript. U.D. performed the immunofluorescence experiments and analyses in cultured cells, and conducted the viability assays involving endocytosis inhibitors. B.C. helped with the organoid experiments, Y.T. analyzed the single-cell RNA sequence data, Y.M. performed the tether force experiments. H.Q. helped with RFP labeling, J.P. and L.R.S. helped with iPS-derived cardiomyocytes, C.K. and L.E.N. oversaw the project.

Competing interests:

L.E.N. is a founder, shareholder, President, and CEO of Humacyte, Inc and serves on Humacyte's Board of Directors. L.E.N.'s spouse is a shareholder of Humacyte. M.H.K, and H.Q. are shareholders and employees of Humacyte, Inc.

bioRxiv preprint doi: https://doi.org/10.1101/2022.06.14.496195; this version posted June 17, 2022. The copyright holder for this preprint (which was not certified by peer review) is the author/funder. All rights reserved. No reuse allowed without permission.

Fig. 1: Inhibition of endocytosis increases the density of Fas microaggregates on the cell surface.

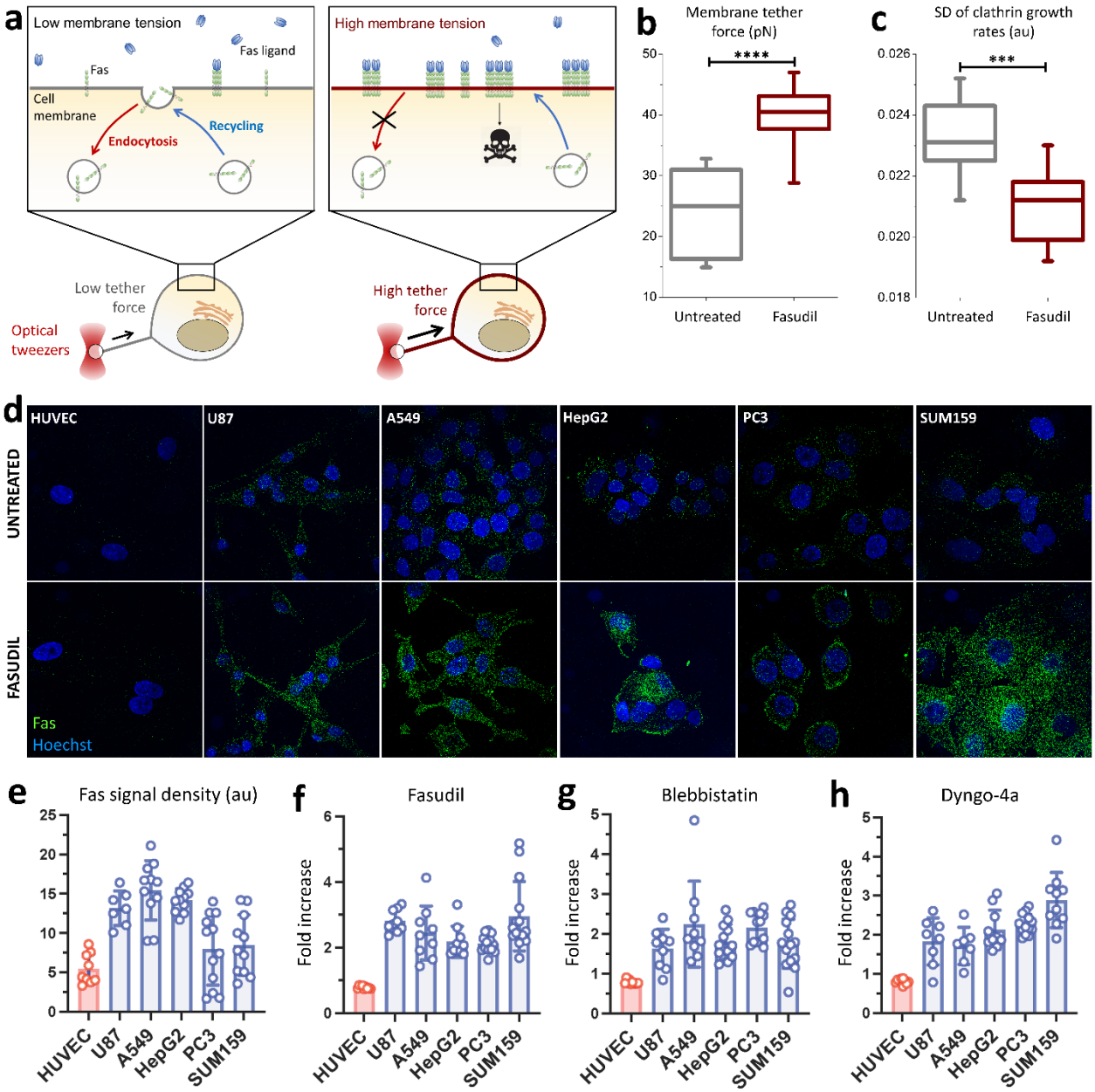

a, We hypothesize that internalization of Fas receptors from the cell surface reduces the sensitivity of cancer cells to Fas-induced apoptosis. Inhibition of endocytic pathways is expected to increase Fas expression on the cell surface and enhance formation of DISC in the presence of FasL. Endocytosis slows down with the increasing plasma membrane tension, which can be quantified by membrane tether force measurements. **b,** SUM159 cells treated with 40 μM Fasudil have significantly higher membrane tension. N_{cells} = 19 (untreated), N_{cells} = 28 (Fasudil). **c,** Clathrin-mediated endocytosis dynamics in SUM159 cells reduce significantly upon 40 μM Fasudil treatment (****: $p<0.0001$, ***: $p<0.001$; two-tailed t-test). N_{cells} = 14, N_{events} = 84230. **d,** Immunofluorescence assays show the increasing Fas microaggregate formation in cancer cells (U87, A549, HepG2, PC3 & SUM159) treated with Fasudil (lower panel). **e,** Relative immunofluorescence signal density obtained from Fas microaggregates are shown for different cells. 40μM Fasudil (**f**), 10 μM blebbistatin (**g**) or 5 μM dyngo-4a (**h**) treatment for 2 hours results in ~2-fold increase in the Fas microaggregate signal in cancer cells.

bioRxiv preprint doi: https://doi.org/10.1101/2022.06.14.496195; this version posted June 17, 2022. The copyright holder for this preprint (which was not certified by peer review) is the author/funder. All rights reserved. No reuse allowed without permission.

Fig. 2: Inhibition of endocytosis sensitizes cancer cells to exogenous FasL.

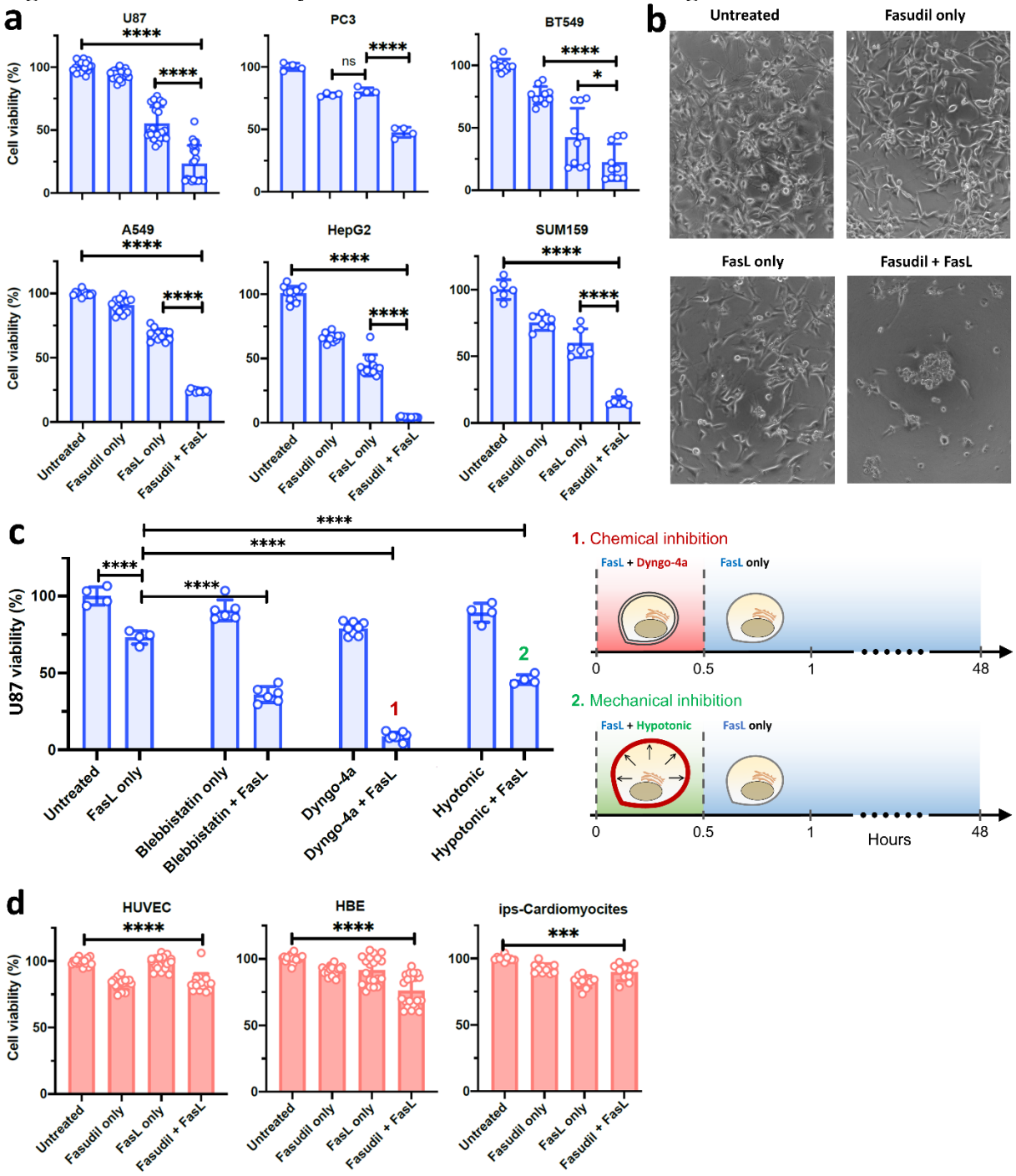

a, Exogenous FasL (400 ng/mL) decreased cell viability significantly in U87, PC3, BT549, A549, HepG2 and SUM159 cancer cells when combined with 40 µM Fasudil. **b,** Representative light microscopy images of U87 cells showing the effect of Fasudil - FasL combination. For the other cancer cell types see Fig. S3. **c,** Similar to Fasudil, blebbistatin (10 µM) reduced U87 viability synergistically with FasL. Inhibition of endocytosis for 0.5 hours by dyngo-4a (1) or hypotonic medium (2) increased sensitivity of U87 cells to FasL substantially. **d,** Viability of HUVECs, HBEs, and iPS-Cardiomyocytes did decrease significantly with Fasudil – FasL treatment, but this decrease was not as dramatic as in cancer cells (****: $p<0.0001$, ***: $p<0.001$, **: $p<0.01$; *: $p<0.05$; ordinary one-way ANOVA, Tukey's multiple comparisons test).

bioRxiv preprint doi: https://doi.org/10.1101/2022.06.14.496195; this version posted June 17, 2022. The copyright holder for this preprint (which was not certified by peer review) is the author/funder. All rights reserved. No reuse allowed without permission.

Fig. 3: Fas-mediated apoptosis in glioblastoma brain organoid model.

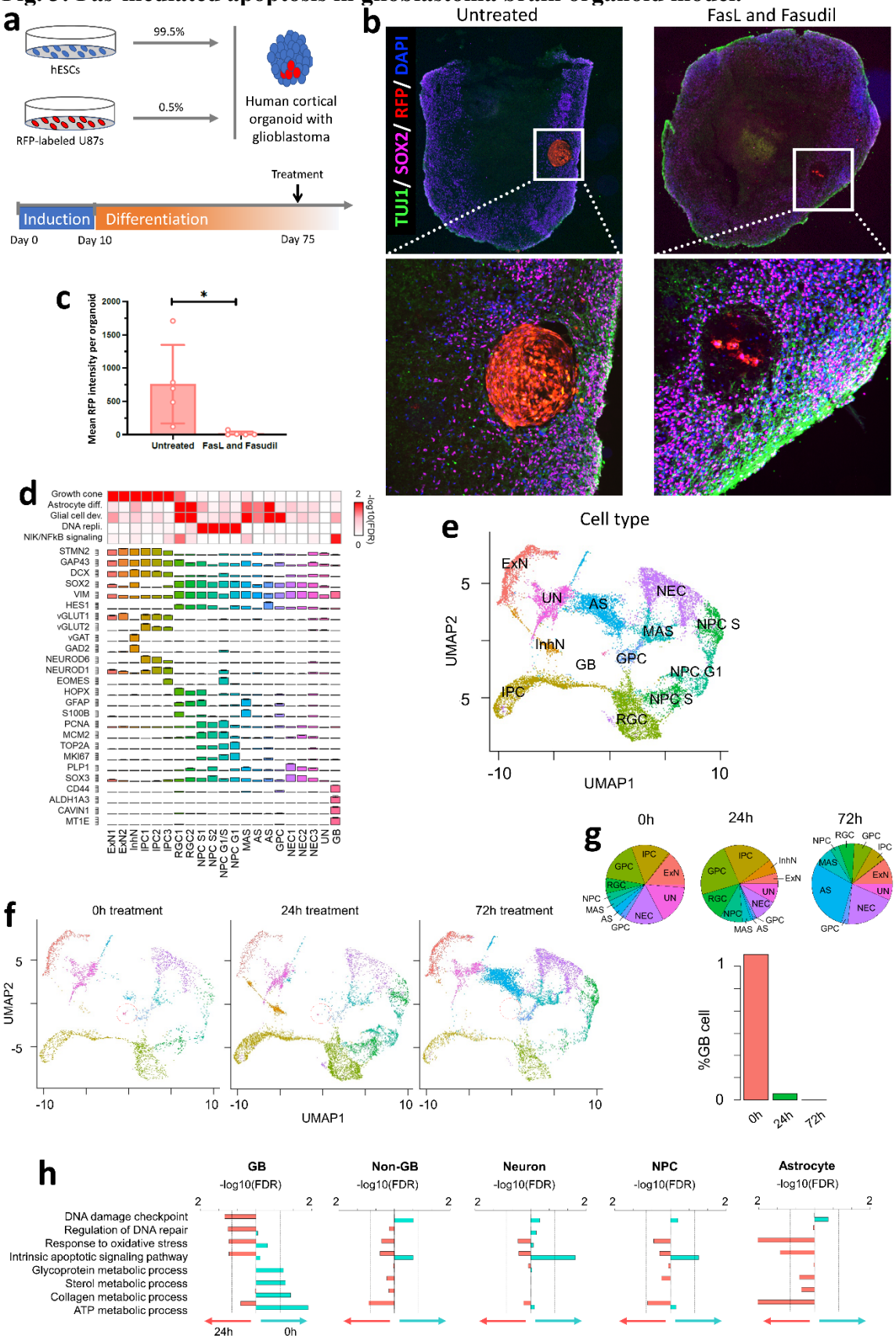

bioRxiv preprint doi: https://doi.org/10.1101/2022.06.14.496195; this version posted June 17, 2022. The copyright holder for this preprint (which was not certified by peer review) is the author/funder. All rights reserved. No reuse allowed without permission.

a, Cortical brain organoids were formed by mixing hESCs with RFP expressing U87 glioblastoma cells with 99.5% and 0.5%, respectively. **b & c,** When 75-day-old organoids containing U87 were treated with Fasudil - Fas ligand combination, the RFP-expressing regions were almost disappeared on day-78 ($p = 0.022$; unpaired t-test). **d & e,** Cell types in UMAP plot of glioblastoma brain organoids. ExN: Excitatory neuron, InhN: Inhibitory neuron, IPC: Intermediate progenitor cell, RGC: Radial glia cell, NPC: Neuronal progenitor cell, MAS: Mature astrocyte, AS: Astrocyte, GPC: Glial progenitor cell, NEC: Neuroepithelial cell, UN: Unknown, GB: Glioblastoma. **f,** UMAP plots of glioblastoma brain organoids at t = 0, 24, and 72 hours of treatment with Fasudil - FasL combination shows that the glioblastoma cluster (encircled in red) gets smaller and disappears with time. **g,** Portions of varying cell types in the organoid at the three different time points. The portion of the GB cells approaches zero after 72 hours of treatment. **h,** After 24 hours of treatment with Fasudil - FasL combination, genes related to apoptotic pathways, DNA damage, and oxidative stress increased in GB cells while genes related to metabolic processes decreased.

bioRxiv preprint doi: https://doi.org/10.1101/2022.06.14.496195; this version posted June 17, 2022. The copyright holder for this preprint (which was not certified by peer review) is the author/funder. All rights reserved. No reuse allowed without permission.

Fig. 4: Fasudil - FasL combination treatment of U-87 glioblastoma *in vivo*.

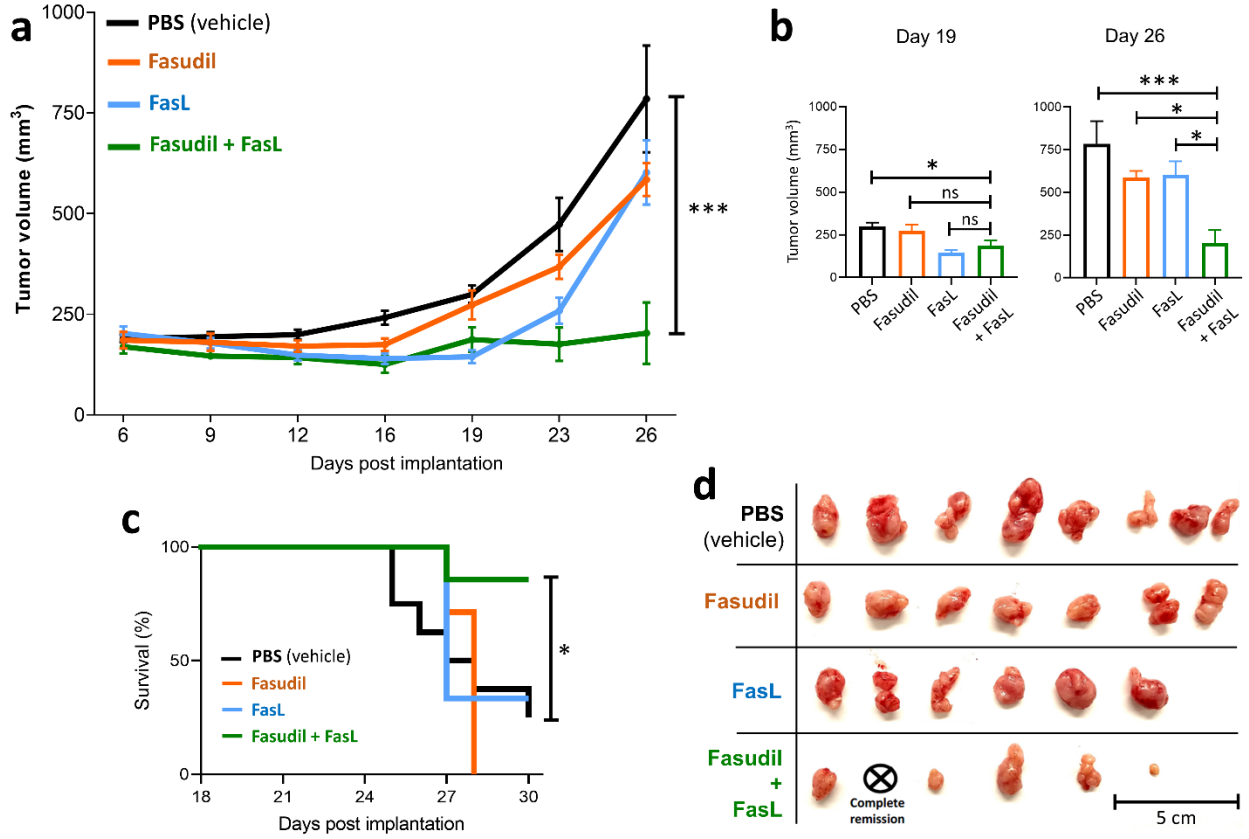

a & b, Tumor sizes in Fasudil - FasL combination group was significantly smaller than those in any other group at the end of the treatment, i.e., 26 days post implantation (***: $p<0.001$, **: $p<0.01$; *: $p<0.05$; ordinary one-way ANOVA, Tukey's multiple comparisons test). **c,** The survival probability in Fasudil - FasL combination group was significantly higher than any group [Log-rank (Mantel-Cox) test; Combination – PBS: $p=0.022$; Combination – Fasudil: $p=0.006$; Combination – FasL: $p=0.048$]. **d,** Extracted tumors one month after the initiation. The tumor in one of mice in Fasudil - FasL combination group was completely cured.

bioRxiv preprint doi: https://doi.org/10.1101/2022.06.14.496195; this version posted June 17, 2022. The copyright holder for this preprint (which was not certified by peer review) is the author/funder. All rights reserved. No reuse allowed without permission.

Supplementary Figures

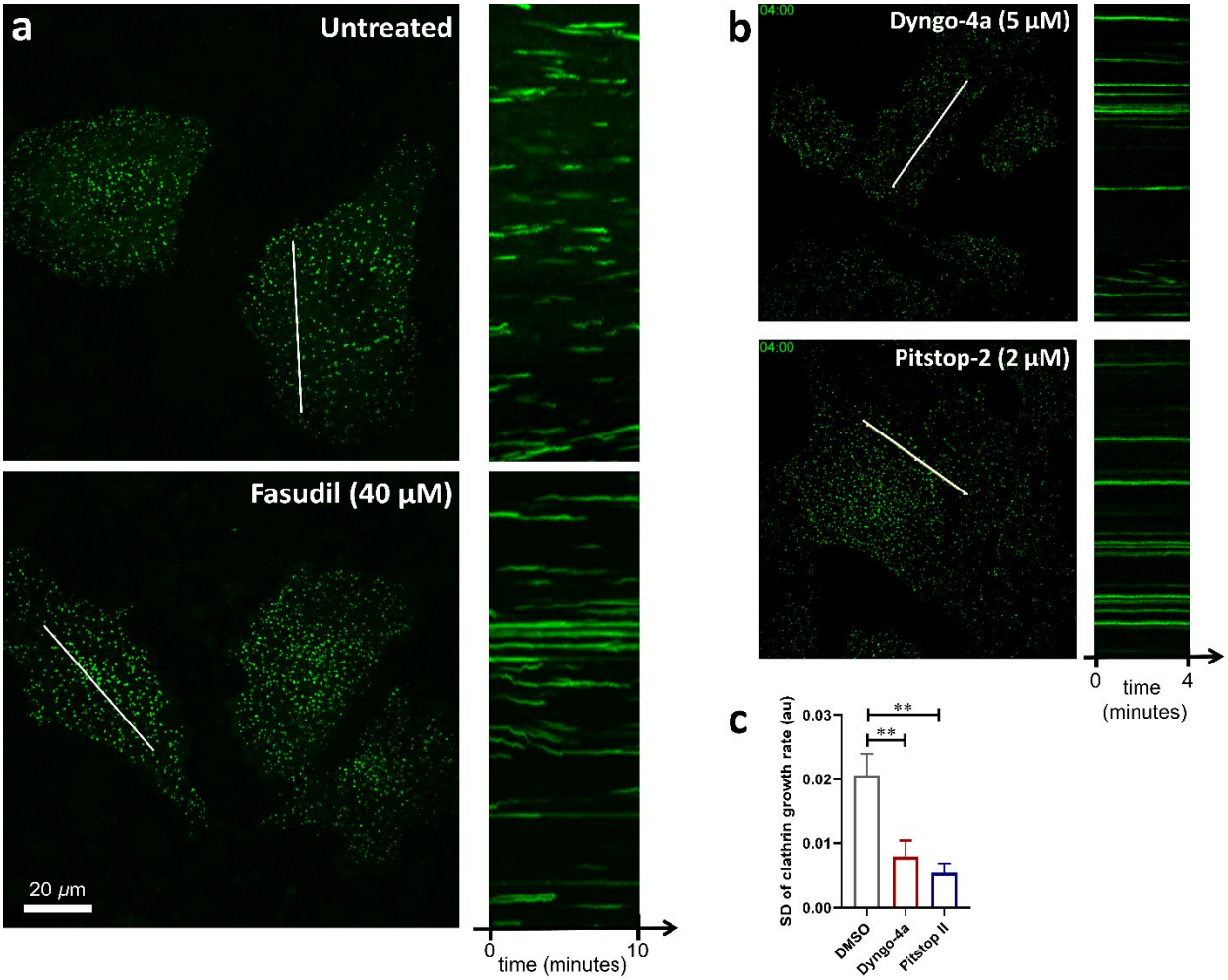

Supplementary figure 1: a, Endocytic clathrin coats are imaged at the ventral surface of live SUM159 cells (genome edited to express AP2-EGFP) untreated (upper) or treated with 40 µM Fasudil for two hours (lower). Kymographs obtained along the marked regions show clathrin-mediated endocytosis dynamics, where the short streaks represent fast endocytic events, and the streaks get longer as endocytosis dynamics slow down. **b,** Kymographs represent the clathrin-mediated endocytosis dynamics in SUM159 cells treated with 5 µM dyngo-4a (upper) or 2 µM pitstop-2 (lower). **c,** Standard deviation (SD) of clathrin coat growth rates are shown control (DMSO, N_{cells} = 11, N_{events} = 29500), and dyngo-4a (5 µM; N_{cells}= 7, N_{events} = 17883) and pitstop-2 (2 µM; N_{cells} = 8, N_{events} = 15903) treated cells ($p<0.01$; ordinary one-way ANOVA, Tukey's multiple comparisons test).

bioRxiv preprint doi: https://doi.org/10.1101/2022.06.14.496195; this version posted June 17, 2022. The copyright holder for this preprint (which was not certified by peer review) is the author/funder. All rights reserved. No reuse allowed without permission.

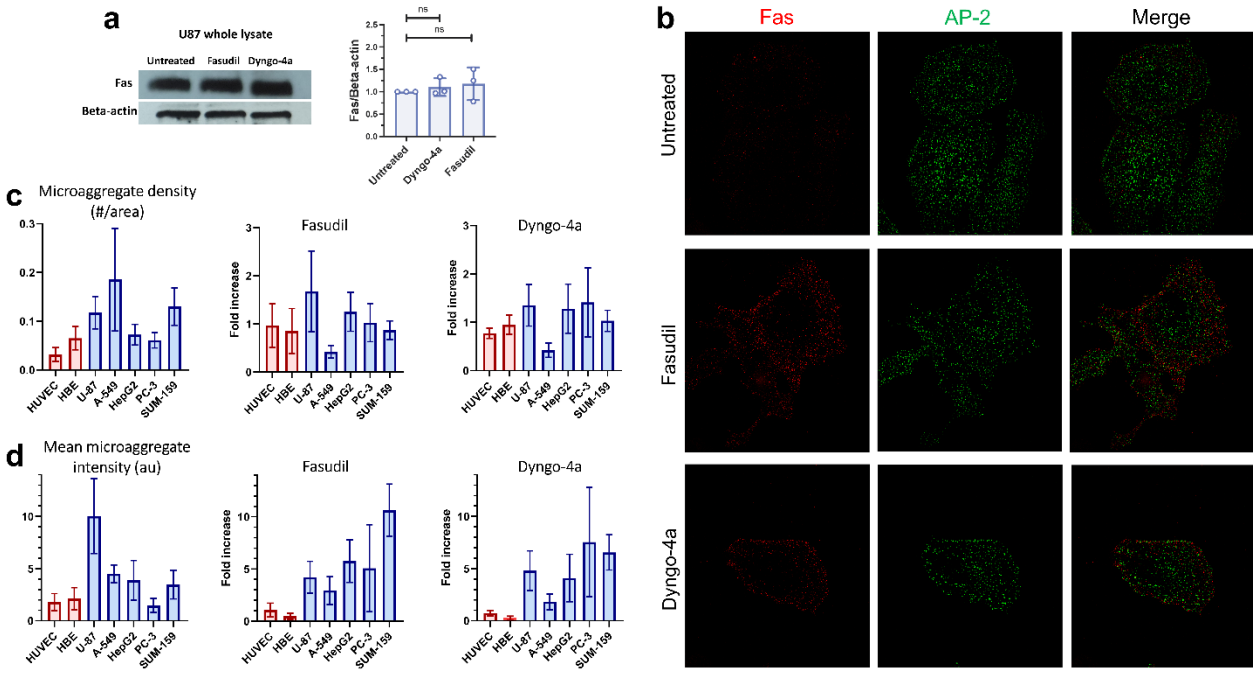

Supplementary figure 2: a, Western blot shows that Fas protein in whole lysates of U87 cells did not change significantly with either 40 µM Fasudil or 5 µM dyngo-4a treatment for 2 hours. **b,** We used spinning disk confocal fluorescence microscopy to image Fas microaggregates exclusively at the ventral/bottom surface of SUM159 cells that are genome edited to express AP2-EGFP to mark endocytic clathrin coats at the plasma membrane. We used AP2-EGFP signal to verify that the image plane coincides with the plasma membrane in these assays. **c,** Density of Fas microaggregates (mean ± stdev) are shown for different cells (left). 40 µM Fasudil (middle) or 5 µM dyngo-4a (right) treatment for 2 hours did not result in significant increase in any of the cell types. **d,** Mean fluorescence intensity of Fas microaggregates (mean ± stdev) shown for different cells (left). 40 µM Fasudil (middle) or 5 µM dyngo-4a (right) treatment for 2 hours did not increase the intensity of Fas microaggregates in HUVEC and HBE cells. Whereas in cancer cells (U87, A549, HepG2, PC3 and SUM159) the increase was substantial.

bioRxiv preprint doi: https://doi.org/10.1101/2022.06.14.496195; this version posted June 17, 2022. The copyright holder for this preprint (which was not certified by peer review) is the author/funder. All rights reserved. No reuse allowed without permission.

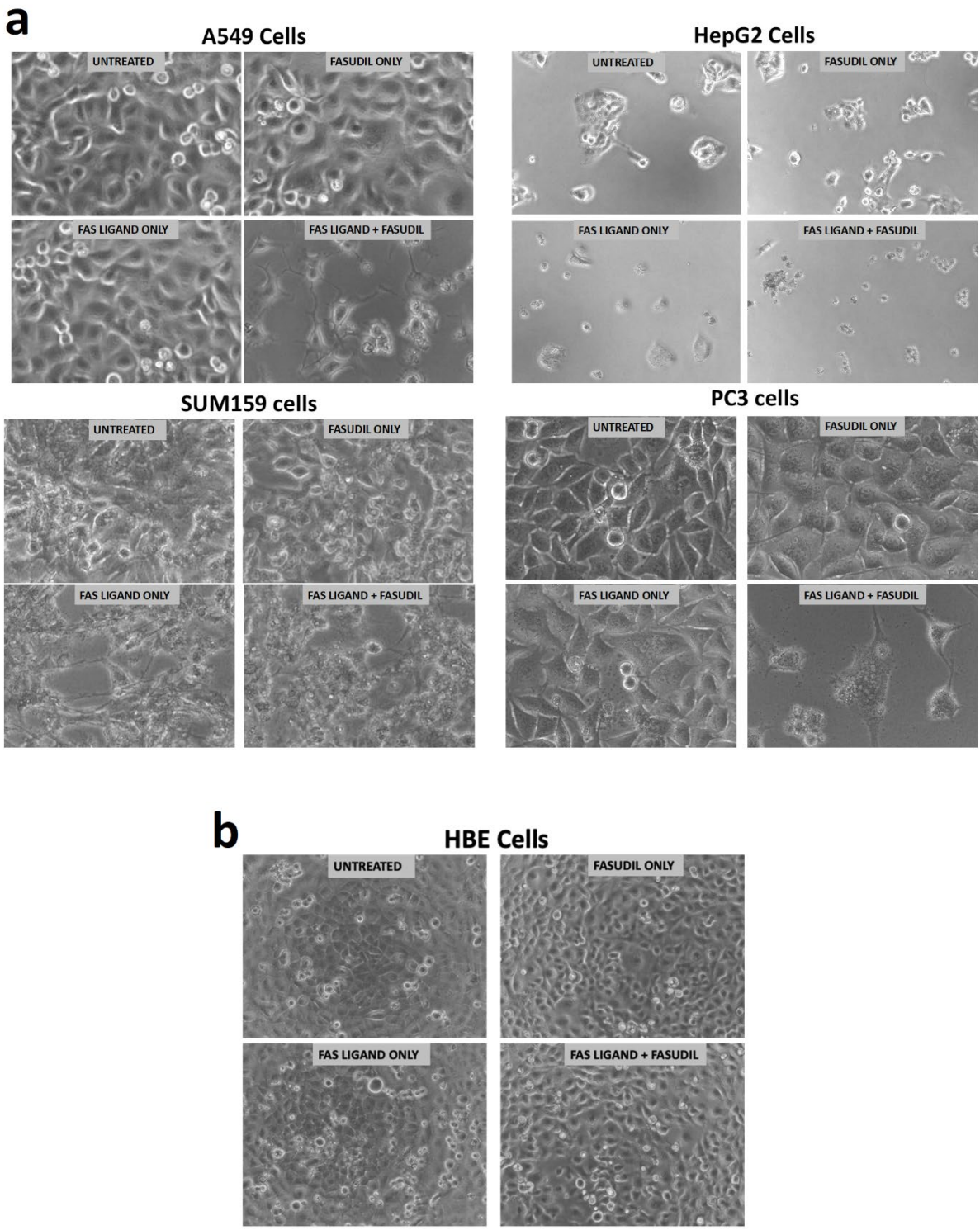

Supplementary figure 3: a, Bright field images of lung cancer cells (A549), liver cancer cells (HepG2), triple negative breast cancer cells (SUM159), and prostate cancer (PC3) shows the dramatic apoptotic effect of Fasudil - FasL combination after 48 hours of treatment. **b,** Unlike cancer cells, human bronchial epithelial (HBE) cells do not express the dramatic apoptotic response to Fasudil - FasL combination.

bioRxiv preprint doi: https://doi.org/10.1101/2022.06.14.496195; this version posted June 17, 2022. The copyright holder for this preprint (which was not certified by peer review) is the author/funder. All rights reserved. No reuse allowed without permission.

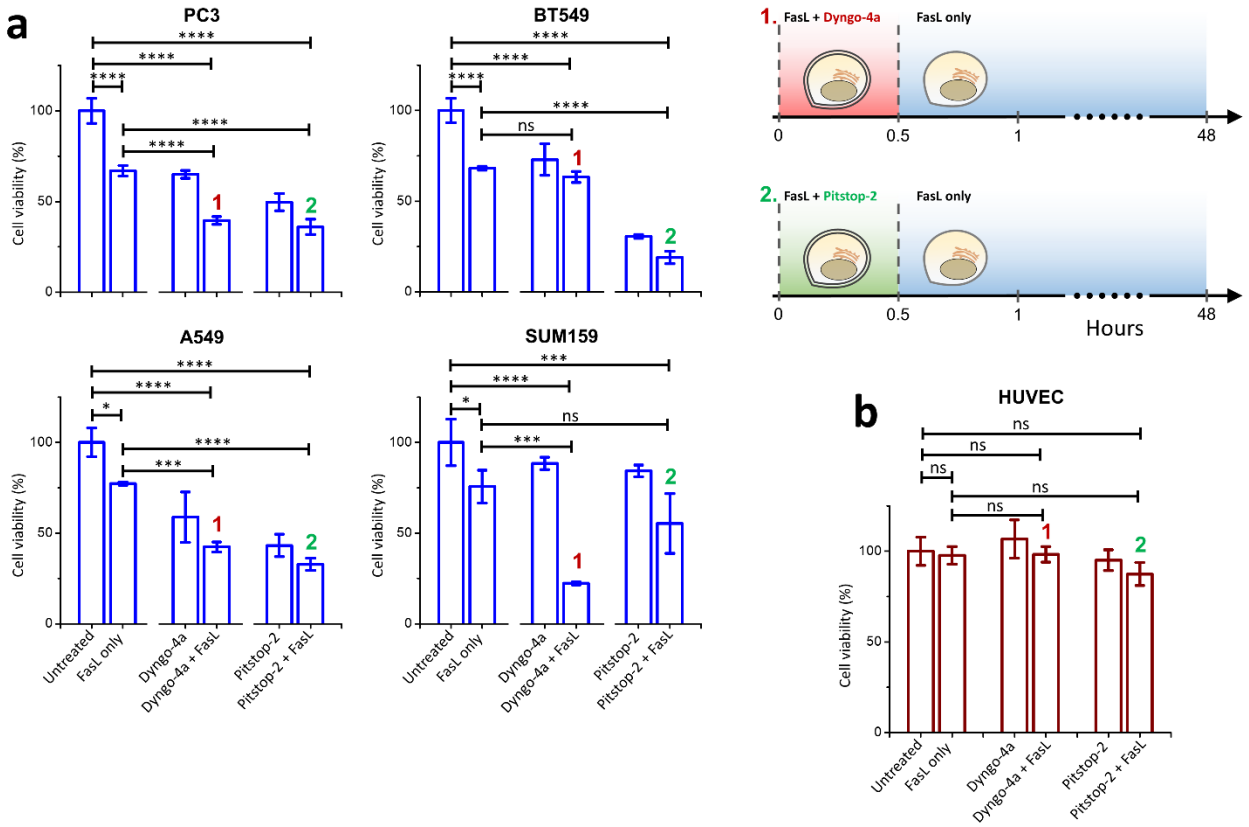

Supplementary figure 4: a, Inhibition of endocytosis for 0.5 hours by dyngo-4a (1) or pitstop-2 (2) increased sensitivity of cancer cells to FasL substantially. **b,** Viability of HUVECs did not change significantly with either dyngo-4a – FasL or pitstop-2 – FasL combination (****: p<0.0001, ***: p<0.001, **: p<0.01; *: p<0.05; ordinary one-way ANOVA, Tukey's multiple comparisons test).

bioRxiv preprint doi: https://doi.org/10.1101/2022.06.14.496195; this version posted June 17, 2022. The copyright holder for this preprint (which was not certified by peer review) is the author/funder. All rights reserved. No reuse allowed without permission.

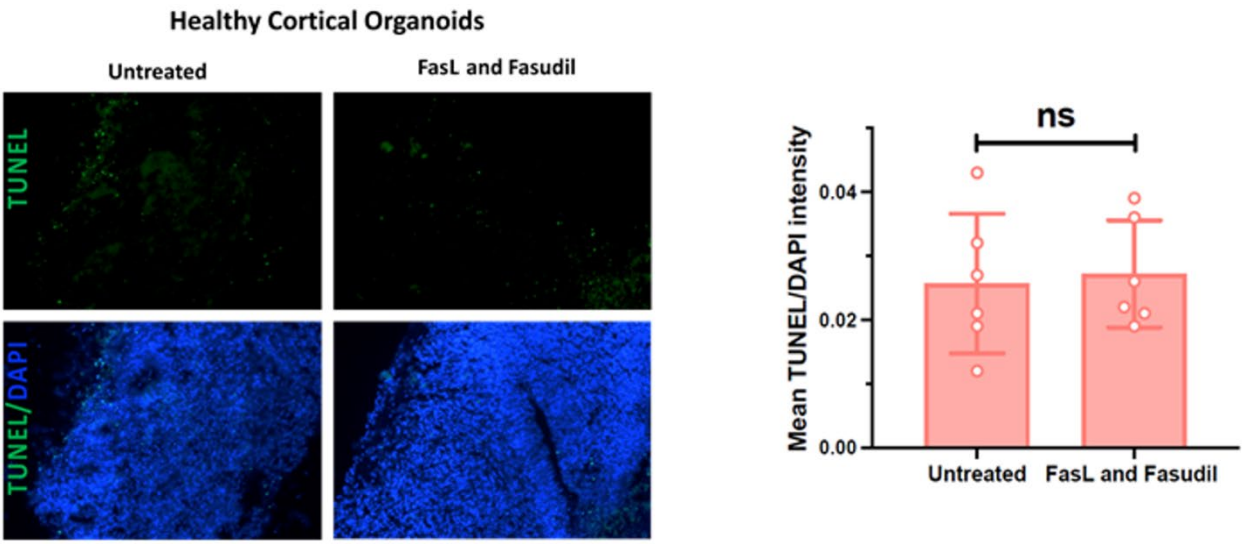

Supplementary figure 5: When 78-day-old healthy organoids were treated with Fasudil – FasL combination the ratio of the number of TUNEL+ cells to total number of nuclei was not significantly different than untreated group ($p = 0.79$; unpaired t test).

bioRxiv preprint doi: https://doi.org/10.1101/2022.06.14.496195; this version posted June 17, 2022. The copyright holder for this preprint (which was not certified by peer review) is the author/funder. All rights reserved. No reuse allowed without permission.

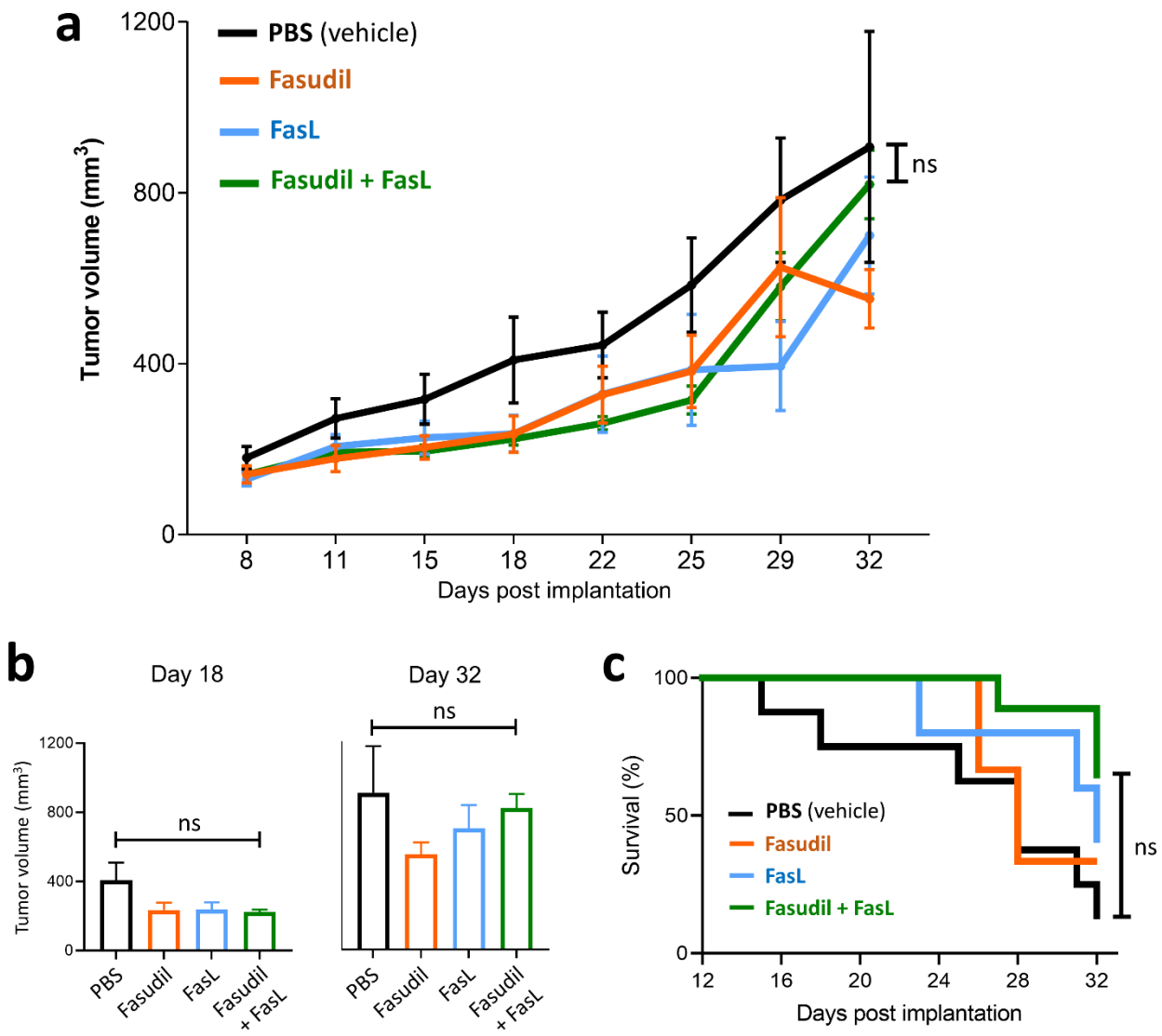

Supplementary figure 6: Intraperitoneal delivery of different treatments did not result in significant difference in the tumor size (**a** & **b**; ordinary one-way ANOVA, Tukey's multiple comparisons test) or survival (**c;** log-rank (Mantel-Cox) test). Overall, FasL-Fasudil combination performed better than PBS but the difference was insignificant.

bioRxiv preprint doi: https://doi.org/10.1101/2022.06.14.496195; this version posted June 17, 2022. The copyright holder for this preprint (which was not certified by peer review) is the author/funder. All rights reserved. No reuse allowed without permission.

Supplementary Videos:

Supplementary video 1: Z-stack acquired by spinning disk confocal imaging shows the surface localization of Fas (red) in a SUM159 cell genome edited to express AP2-EGFP (green).

Supplementary video 2: Untreated iPS-cardiomyocyte monolayer that is spontaneously contracting on the tissue culture plastic.

Supplementary video 3: 48 hours of treatment with combinations of Fasudil - FasL combination did not affect the contraction ability of iPS-cardiomyocyte monolayer.